Narrow Emission from $Rb_3Sb_2I_9$ Nanoparticles

Andrew Johnston, Filip Dinic, Petar Todorović, Bin Chen, Laxmi Kishore Sagar, Makhsud I. Saidaminov, Sjoerd Hoogland, Oleksandr Voznyy,* and Edward H. Sargent*

Metal halide perovskites have gained attention for their optoelectronic properties and are employed as the active layer in solar cells, light-emitting diodes, and photodetectors. However, the use of lead in the best-performing perovskite devices may limit their wider application. Prior reports of lead-free perovskite nanoparticles have exhibited linewidths more than twice as wide as their lead-halide counterparts, limiting their attainable color gamut. Here the solution synthesis of lead-free $Rb_3Sb_2I_9$ nanoplatelets and single crystals is reported; the single crystals exhibit broad (full-width at half-maximum (FWHM) = 75 nm) photoluminescence centered at 635 nm, while the nanoplatelets exhibit narrow emission (FWHM = 21 nm) at 512 nm. The photoluminescence quantum yield of both the single crystals and nanoplatelets is low and the present demonstration of the narrowest emission among all lead-free perovskites reported to date motivates further study of how these and related materials can achieve further-enhanced brightness.

Metal halide perovskites have seen significant interest for their applications in optoelectronic devices.[1–9] Perovskite nanocrystals (NCs) exhibit excellent emissive properties, including spectral tunability, high photoluminescence quantum yield (PLQY), and narrow emission linewidths.[10–13] The best performing perovskite devices and materials contain lead; and this can restrict application in certain consumer applications.[14] Replacing lead with a divalent cation such as Sn^{2+}, Ge^{2+}, and Ca^{2+} has been explored with some success,[15–22] but in general these substitutions have so far limited the performance and stability of the final devices.[17,23]

It is also possible to replace Pb with atoms of differing oxidation states that share the ns^2 hybridization state of Pb^{2+}, such as Sb^{3+}, and Bi^{3+};[18] the trivalent cation necessitates that the stoichiometry of the remaining components of the perovskite structure differs to maintain charge balance. The resulting material has the chemical formula $A_3B_2X_9$, in which A and X are a small monovalent cation and halide, respectively, and B is the Bi^{3+} or Sb^{3+} cation. Several of these materials have been predicted to have a direct bandgap at an energy suitable for optoelectronic applications[24] and have subsequently been explored as thin films for device applications.[25–29]

Reports of nanocrystal syntheses of $A_3B_2X_9$ materials have shown efficiencies ranging from <1% to 40% PLQY[30–33] and are sensitive to the synthesis conditions.[30] As in lead-halide perovskite NCs, the lead-free materials display spectral tunability and exhibit the highest PLQY values when Br or Cl is incorporated as the halide, resulting in deep-blue or UV emission.

$A_3B_2X_9$ materials can form two different phases: a dimer structure with face-sharing octahedra (indirect bandgap) or a layered structure with corner-sharing octahedra (direct bandgap).[34] The formation of the dimer phase (indirect bandgap) of $Cs_3Sb_2I_9$ is favored over the layered phase, but it has been demonstrated that the incorporation of Cl^- can favor the layered phase.[29] This may contribute to the improved PLQY observed in the Br- and Cl-incorporating nanocrystals: the smaller halides are more likely to form the direct-bandgap layered phase. When a smaller cation such as Rb is introduced in place of the Cs, the layered phase becomes favored over the dimer phase for both Br- and I-variants, enabling longer wavelengths of emission.[34]

$A_3B_2X_9$ nanocrystals reported thus far have exhibited wider (≈2x) emission linewidths than their lead-halide perovskite counterparts. The nanocrystals take the form of quantum dots and are confined in all three dimensions; the size distribution leads to a distribution of energy levels across the population of quantum dots. This contributes to inhomogeneous broadening of the emission linewidth, limiting the color purity of the final product. Color purity is an important consideration for display applications, as it determines the attainable range of the color gamut. For nanocrystal displays, the full-width at half-maximum (FWHM) for each of the red, blue, and green (RBG) emitters should be no greater than 30 nm so that these can fulfill the specification on color rendering index developed by the International Commission for Illumination.[35] The color limit is improved as the linewidth of each of the RBG emitters in a display decreases.[36]

A. Johnston, P. Todorović, Dr. B. Chen, Dr. L. K. Sagar,
Dr. M. I. Saidaminov, Dr. S. Hoogland, Prof. E. H. Sargent
Department of Electrical and Computer Engineering
University of Toronto
Toronto, Ontario M5S 1A4, Canada
E-mail: ted.sargent@utoronto.ca
F. Dinic, Prof. O. Voznyy
Department of Physical and Environmental Sciences
University of Toronto Scarborough
Scarborough, Ontario M1C 1A4, Canada
E-mail: o.voznyy@utoronto.ca

The ORCID identification number(s) for the author(s) of this article can be found under https://doi.org/10.1002/adom.201901606.

**ADVANCED
SCIENCE NEWS**
www.advancedsciencenews.com

**ADVANCED
OPTICAL
MATERIALS**
www.advopticalmat.de

Here we report the synthesis of $Rb_3Sb_2I_9$ (RSI) nanoplatelets using an antisolvent technique. The nanoplatelets exhibit a sharp emission peak at 512 nm (FWHM = 21 nm), which is the narrowest observed among lead-free perovskite-like nanocrystals. We attribute the narrow emission to the formation of nanoplatelets rather than quantum dots: nanoplatelets have a narrower spontaneous emission spectra and suppressed inhomogeneous broadening.[37–39]

We first grow large single crystals of bulk $Rb_3Sb_2I_9$ using an adapted solution-processed technique[40] and confirm the structural properties with both X-ray and neutron diffraction. We study the bulk optical properties of the RSI single crystals, including photoluminescence (PL) and absorption. We then synthesize RSI nanoplatelets and confirm the structure with powder X-ray diffraction (XRD) and X-ray photoelectron spectroscopy (XPS). Using transmission electron microscopy (TEM), we observe large (width = 30 nm) sheets of $Rb_3Sb_2I_9$.

We first synthesized large single crystals of $Rb_3Sb_2I_9$ to study its material properties. The single crystals were synthesized by dissolving the precursor salts (RbI and SbI_3) in a stoichiometric ratio in hydroiodic acid (HI) at high temperatures, and then slowly cooling the solution to precipitate the single crystals, adapted from a previously reported technique to grow lead-halide perovskite single crystals.[40] We analyzed the single crystal with both X-ray and neutron diffraction to identify the crystal structure. The single crystal shows a monoclinic structure and belongs to the space group *P 21/n*. The unit cell parameters are listed in **Table 1**; the parameters are consistent for both the X-ray and neutron diffraction. $Rb_3Sb_2I_9$ favors a corner-sharing layered crystal structure that has been reported previously to possess a direct bandgap.[34] The powder XRD profile of the single crystal indicates a preferential crystal growth orientation along the *c* axis, as evidenced by the strong diffraction peaks at 2Θ values of 17.2° and 25.93° corresponding to the (004) and (006) lattice planes, respectively. We then measured the absorption and photoluminescence properties of the single crystal, seen in **Figure 1**. From the Tauc plot (Figure 1c), we extract a direct bandgap of 1.95 eV, consistent with other reports and density functional theory (DFT) simulations.[24,27,34]

The crystal exhibits broad photoluminescence emission centered at 635 nm; the quantum yield of the single crystal is weak, and we attribute the shoulder observed in the emission spectrum at 550 nm to reabsorption within the crystal. This has been observed before in perovskite single crystals[5] and is not present in the PL spectrum of thin films of RSI (Figure S1, Supporting Information). We observed no 2-photon induced emission from the single crystal. When the crystal was exfoliated, we observed that the shoulder disappeared, indicating that the shoulder is indeed due to reabsorption (Figure S1, Supporting Information). To help elucidate the weak emission properties, we measured time-resolved photoluminescence decay, displayed as the inset of Figure 1c. The decay was fit to a biexponential curve (Experimental Section), where the fast component is associated with nonradiative recombination and the slow component the radiative recombination; calculating the PLQY from the resulting fit parameters constants agrees with the measured PLQY ($\approx$0.1%).[41] The extracted fit parameters are given in **Table 2**. From the fit, it is evident that the fast, nonradiative recombination (τ = 1.2 ns) dominates the signal. The fast recombination points to the presence of defects within the single crystal as well as a weak exciton binding energy, which has been reported before for this material.[28] However, the quantum yield of bulk lead-halide perovskite single crystals is also low, and yet the lead-halide perovskite nanocrystals of this still show excellent PLQY and photoluminescent spectra. We thus sought to synthesize nanocrystals of this material to explore whether quantum confinement would yield improvements in the emissive properties of this material.

To improve the low PLQY and broad emission of the bulk variant of RSI, we synthesized RSI nanocrystals. In standard perovskite nanocrystal synthesis, a hot-injection method is used in which the A-site cation reacts with oleic acid (OA) to form an oleate precursor, which is then injected into a solution of solubilized BX_2 salt precursor.[10] While this method has proved successful with lead-halide perovskites, it is not effective for $A_3B_2X_9$ materials: the volatile SbI_3 decomposes before the reaction occurs. We thus adopted an antisolvent ligand-reprecipitation method to synthesize nanoparticles.[31] In this method, the precursor salts are solubilized in a good solvent, and a portion of the precursor solution is then injected into an antisolvent solution in which stabilizing ligands are present. The much lower solubility of the precursor salts in the antisolvent induces precipitation of the salts, which then crystallize and are stabilized by the ligands present in the antisolvent (for details, see the Experimental Section). In addition, we added an ammonium salt ($C_6H_{16}IN$ or $C_8H_{16}IN$) to the precursor solution to improve the stability of the nanoparticles, as is reported in ref. [30]. Upon injection of the precursor solution into the antisolvent, a color change occurred over the course of 1–2 s, indicating that a reaction had occurred. The product was then centrifuged at a low speed, and the unreacted precursor was discarded. This is the first reported synthesis of RSI nanocrystals using the antisolvent method.

To investigate the structural properties of the nanoparticles, we employed XPS and XRD. In both cases, the nanoparticle solution was drop cast onto a glass slide. The XPS results are shown in **Figure 2**a–c. It is clear that the nanoparticles contain Rb, Sb, and I, and the resultant atomic ratio of Rb:Sb:I is 0.25:0.33:0.23. Interestingly, XPS indicates a surplus of Sb and a deficiency of I compared with the precursor ratios: for Sb, we conclude that the nanoparticle surface is Sb-rich, while the high ionization yield of I makes it difficult to quantify with XPS measurements. The Sb-rich surface has been observed in previous reports of $A_3B_2X_9$ materials.[31] We note also that there was a strong presence of the C1s peak in the XPS measurement,

Table 1. Unit cell parameters of RSI single crystals obtained from neutron and X-ray diffraction measurements.

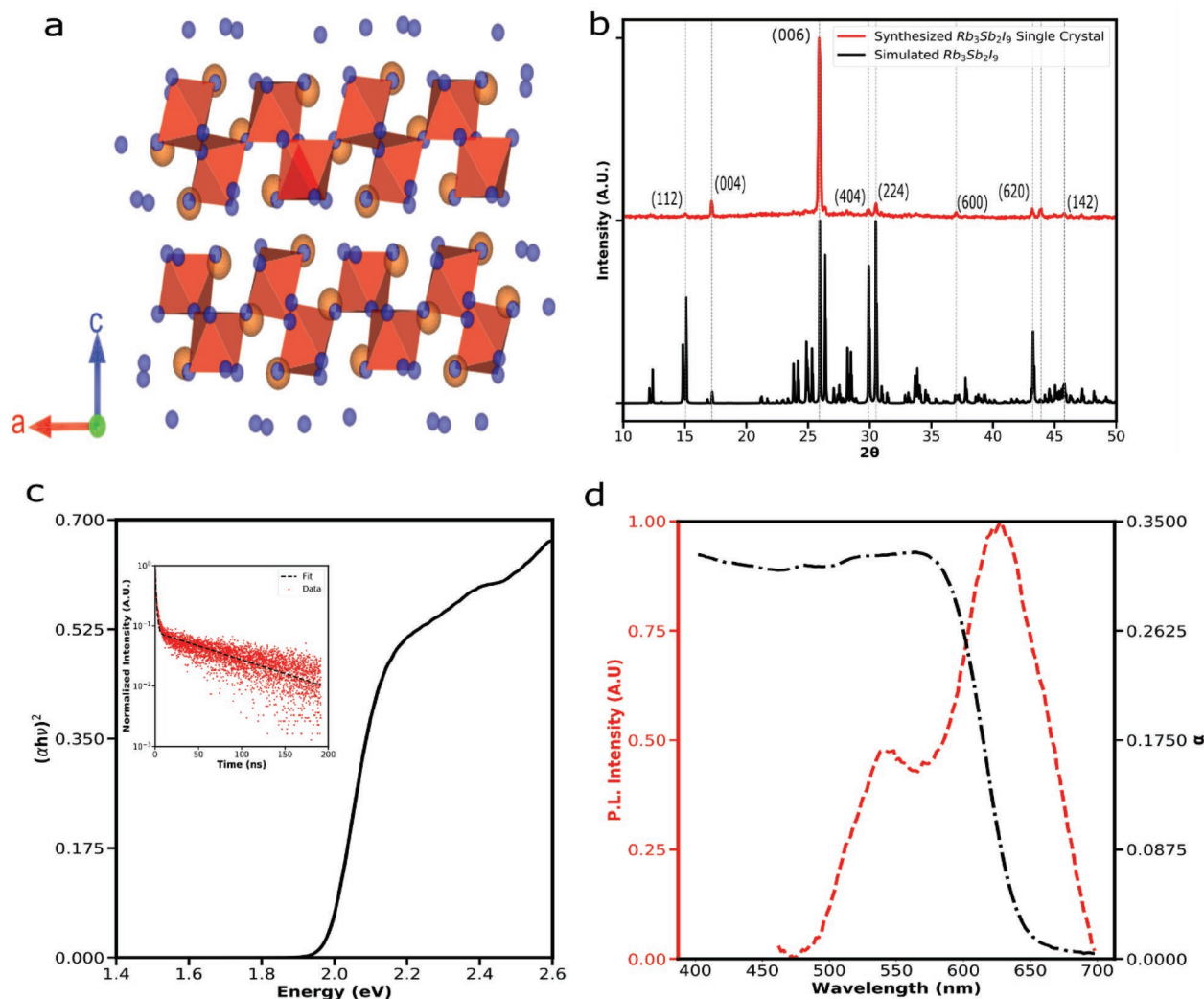|	Neutron diffraction	X-ray diffraction
a [Å]	14.53	14.59
b [Å]	8.174	8.19
c [Å]	20.58	20.58
α	90.0°	90.0°
β	90.53°	90.36°
γ	90.0°	90.0°
Space group	*P 21/n*	*P 21/n*

Figure 1. Characterization of Single Crystal RSI. a) The unit cell of RSI viewed along the *b* axis; the blue spheres represent I, the brown represents Rb, and the red octahedra represent Sb. b) Powder XRD measurement of the synthesized single crystal (red) and the simulated XRD pattern (black). c) Tauc plot of single crystal. Inset shows the PL-decay. d) PL and absorption spectra of the single crystal, showing a broad emission centered at 630 nm.

which we attribute to both carbon contamination and the presence of stabilizing ligands on the surface of the nanoparticles.

The XRD profile obtained from the nanocrystals is seen in Figure 2d and is compared with the simulated XRD profile of RSI single crystals. The XRD analysis suggests that the nanocrystals are RSI where the peaks at 15.16°, 23.82°, 24.72°, and 25.98° match the (112), (214), (313), and (006) planes, respectively. The orientation of the RSI NCs on the glass film appears arbitrary. The unassigned peaks are from unreacted precursor salts SbI_3, RbI, and $C_6H_{16}IN$ (Figure S2, Supporting Information), indicating that there were small amounts of unreacted precursor in the final product. In contrast with the case of lead-halide perovskites, we observe no diffraction corresponding to the (002) or

Table 2. Fit parameters from PL-decay of single crystal of RSI.

	C_1	τ_1 [ns]	C_2	τ_2 [ns]	R^2
Value	0.752	1.2	0.079	94.6	0.94

(004) peaks; the different symmetry and lattice constants of RSI ensure that the (002) and (004) peaks occur at lower angles (8.6° and 17.2°, respectively) and are of lower intensity than the (006) peak (Figure S2, Supporting Information).

To determine the shape of the nanoparticles, we imaged the product using TEM. To ensure minimal organic contamination of the imaged materials, we further washed the nanoparticles by precipitation through centrifugation at a faster speed (13 000 rotations per minute (RPM) for 10 min). The yellow-green precipitate was then redispersed in toluene before being added to the TEM grids.

The TEM images obtained are seen in **Figure 3**a. The TEM analysis indicates that the nanoparticles take the form of nanoplatelets, oriented parallel to the substrate. The high-angle annular dark field images indicate that the nanoplatelets are rectangular but of various widths. The dark regions in the dark field imaging mode represent areas with lower crystallinity or lower atomic mass: in this case it is likely that this is the presence of crystalline defects, as excess organics should have been
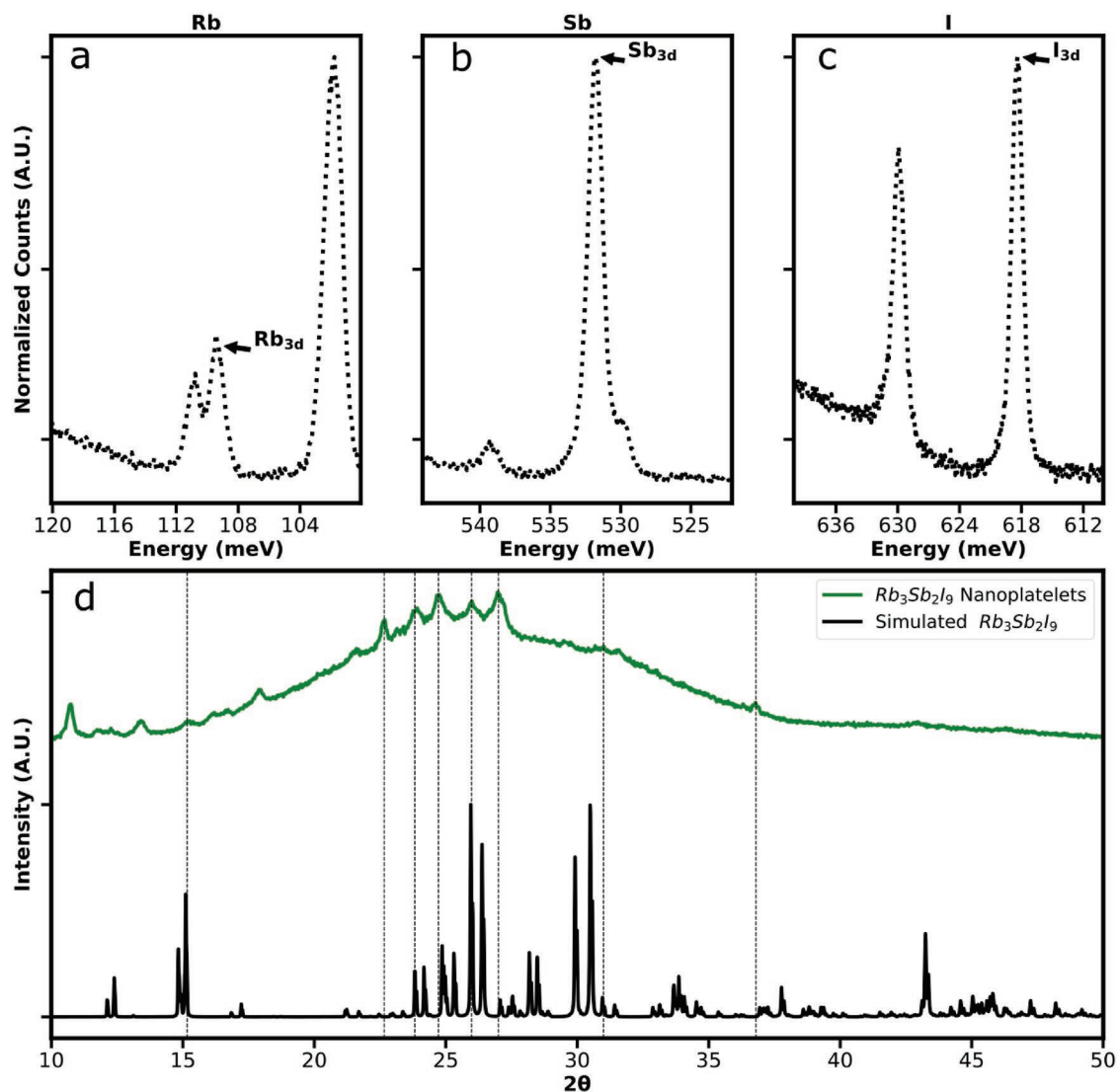
Figure 2. Structural and compositional characterization of RSI nanoplatelets. a–c) XPS results for Rb, Sb, and I detection, respectively. d) XRD profile of the obtained RSI nanoplatelets (green) and the simulated XRD profile (black).

removed with the additional purification step as well as exposure to the electron beam. The presence of such surface defects may contribute to curtailing the photoluminescence quantum yield of the nanoparticles, a point that is discussed further in the section that follows.

A high-resolution TEM (HRTEM) image is shown in Figure 3b, the lattice fringes indicate high crystallinity. The fast Fourier transform (FFT) of this image was fit to the zone (001) RSI, shown in the inset of Figure 3b. A selected area electron diffraction (SAED) image (Figure S3, Supporting Information) was integrated and the resultant intensity profile was plotted in Figure 3d. The integrated intensity was compared with the RSI single crystal XRD: the two profiles are well matched, further corroborating the formation of RSI nanoparticle. TEM size analysis, shown in Figure 3c, indicates a wide array of sizes of the nanoplatelets, ranging from ≈300 to ≈900 nm². The diameters of the nanosheets follow a normal distribution, with an average diameter of 34 ± 5.2 nm and an average area of 550 ± 173.9 nm². The

lateral dimensions of the nanoplatelets are larger than the Bohr radius of perovskite materials (≈12 nm for $CsPbX_3$),[10] indicating that the quantum confinement observed in the emission comes from confinement in the direction normal to the TEM grid. We note that attempts to quantify the thickness of the nanoplatelets with atomic force microscopy (AFM) were unsuccessful due to the roughness of the films formed from the solutions.

We attribute the formation of 2D nanoparticles rather than 0D nanoparticles to formation energy of the two possible phases of RSI. Specifically, the formation of the quasi-2D layered phase is favored over the 0D dimer phase, which we suspect makes the formation of 2D nanoplatelets favored over 0D nanoparticles. This comes from incorporating Rb as the A-site cation rather than the more conventional Cs, since the smaller size of Rb favors the layered phase.[29,34]

We measured the photoluminescence and absorption spectra of the obtained nanoplatelets, shown in **Figure 4**. The nanoparticles exhibit an exceptionally narrow emission centered at
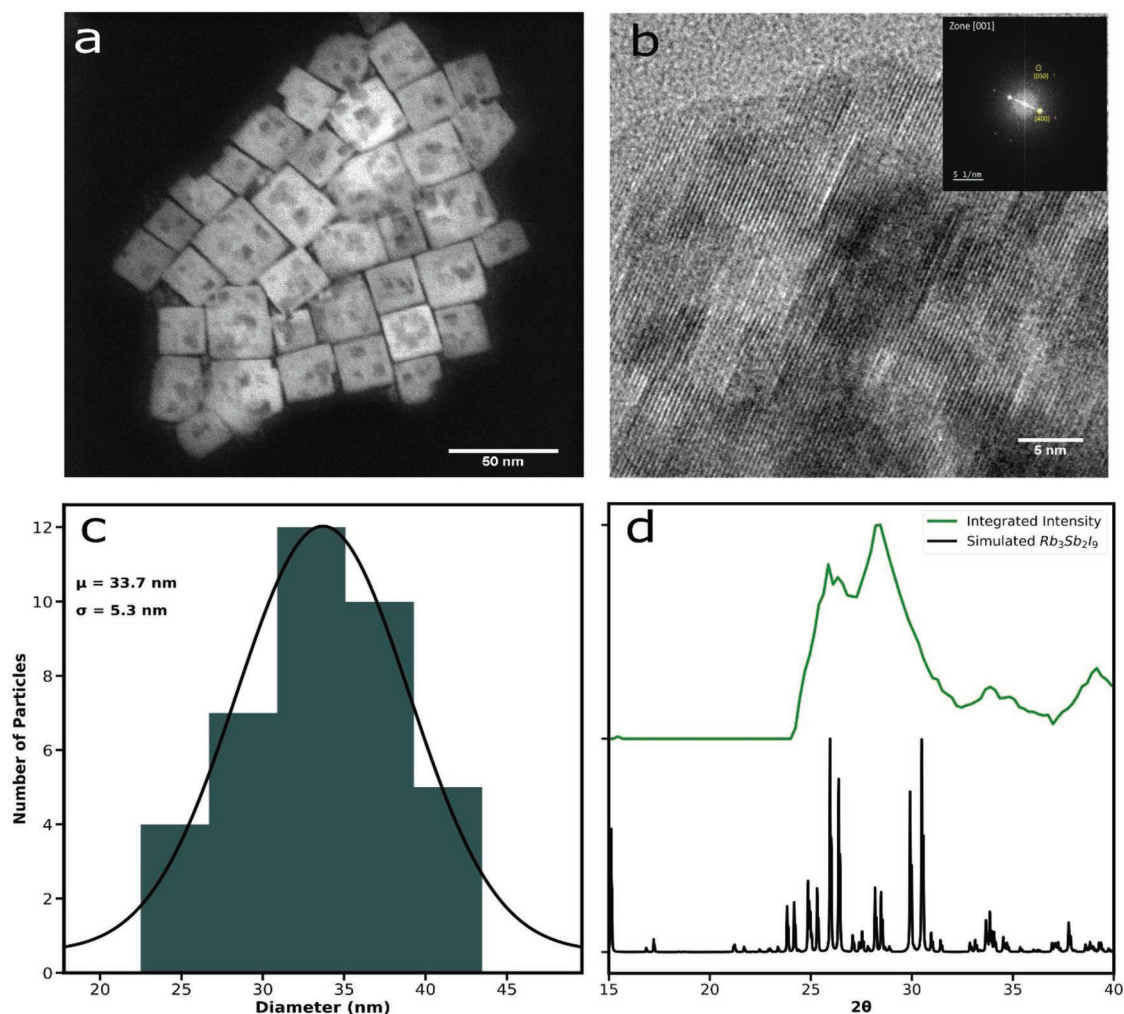
Figure 3. TEM characterization of RSI nanoparticles. a) Dark-field image of the nanoplatelets. b) HRTEM image of the high-resolution of one of the nanoplatelets, and the inset shows the FFT transformation, which can be matched to Zone (001) of RSI. c) Size distribution of the nanoplatelets, with an average diameter of 33.7 nm and a standard deviation of 5.3 nm. d) The angular integrated intensity of the selected area electron diffraction image of the nanoplatelets (green) compared with the simulated XRD pattern (black).

512 nm. The emission peak at 512 nm has an FWHM value of 21 nm, which is consistent with previous reports of perovskite nanoplatelets. To our knowledge, this is the narrowest emission spectra obtained from any $A_3B_2X_9$ perovskite-like material. Narrow linewidths are an essential consideration for color purity, which is necessary to maximize the color gamut available for display applications.[35,36] In addition, the nanoplatelets exhibit an excitonic feature in its absorption spectra at 500 nm. The small Stokes shift is also consistent with previous reports of perovskite nanoplatelets.[42,43] Nanoplatelets can exhibit narrower emission spectra than quantum dots, since the thickness distribution, and therefore the energetic distribution, can be discrete rather than continuous.[43] However, the PLQY of colloidal nanoplatelets is typically lower than that of colloidal quantum dots and often requires detailed screening of synthetic parameters to achieve high PLQYs.[44]

In experiments in which we varied ligand concentration, we did observe emission at different wavelengths (Figure S4, Supporting Information), indicating that the size

of the nanoplatelets and thus the center of emission spectrum was tunable. Indeed, we observed both blue (462 nm) and red (635 nm) emission; however, it was our experience these nanoplatelets were unstable (≈hours in solution) and rapidly degraded. The synthesis yielding the 512 nm emission was more reliable and the particles were stable in solution for an appreciable amount of time (≈2 weeks, in air). Varying the halide composition in lead-halide perovskite nanoparticles results in a modified bandgap.[10] When we substituted iodine with bromine, we observed no emission from the resulting nanoparticles, but acknowledge that a modified synthesis procedure may yield emissive $Rb_3Sb_2Br_9$ nanoparticles.

The photoluminescence quantum yield of the nanocrystals was low (≈0.2%), owing to both the surface defects observed in the TEM images and the strong reabsorption of the nanoparticles due to the low Stokes shift. All optical measurements were performed on solutions of the nanoparticles. We measured the PL-decay of the nanoparticles, seen in Figure 4b, and fit the data to a biexponential curve. As with the single crystal, there is
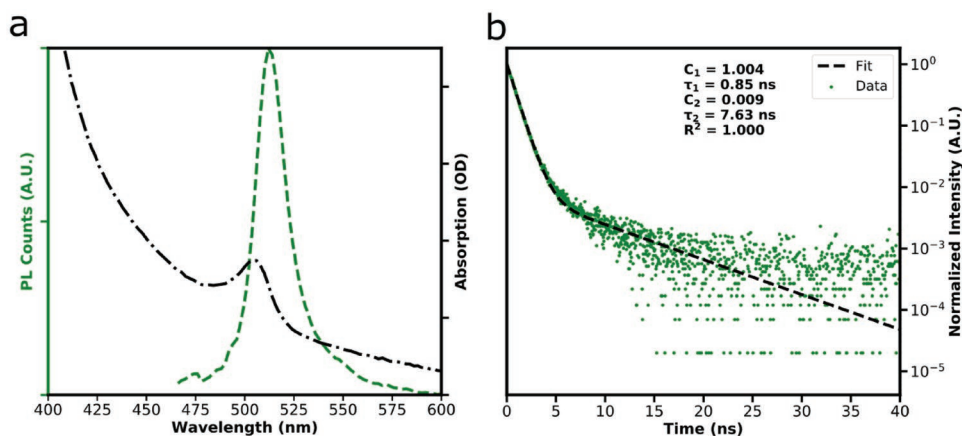
Figure 4. Optical characterization of the RSI nanoparticles. a) shows the photoluminescent spectrum (green), which exhibits a peak emission at 512 nm with an FWHM of 21 nm and the absorption spectrum (black). b) shows the transient PL signal obtained at 512 nm as well as the fit parameters.

a fast and slow component of the decay: the fast, nonradiative component dominates the signal. Power-dependent PL-decay measurements (Figure S7, Supporting Information) show that the fast component is substantially invariant with increasing power and that the slow component becomes faster at higher fluences. This is consistent with the relatively low PLQY observed in the sample. In our future work, we are designing passivation mechanisms to reduce the presence of the surface defects and subsequently improve the PLQY of these lead-free materials.

Nanoplatelets of $Rb_3Sb_2I_9$ synthesized using a simple antisolvent method produced nanoplatelets several tens of nanometers in width and rectangular in shape. We compared the optical properties of the nanoplatelets with those of bulk single crystals of RSI and found that the emission was greatly blueshifted and had a much narrower emission linewidth. The nanoplatelets exhibited the narrowest emission among all lead-free perovskite nanoparticles made to date, with an emission peak at 512 nm with a 21 nm FWHM.

Experimental Section

Synthesis of RSI Nanoparticles: In a typical nanocrystal synthesis, 0.6 mmol of RbI, 0.6 mmol of $C_6H_{16}IN$, and 0.8 mmol of SbI_3 were dissolved in 9.5 mL of acetonitrile and 0.5 mL of dimethylformamide. The precursor solution was stirred for 2 h at room temperature to fully dissolve the precursors. During this time, an antisolvent solution containing 10 mL toluene, 500 µL of OA, and 70 µL of olelyamine was prepared. The precursor solution was filtered prior to reaction to remove any undissolved precursor. 1.0 mL of the filtered precursor solution was added to the vigorously stirring antisolvent solution, upon which the reaction occurred within a few seconds. The product was stirred for an additional minute. To wash, the raw product was centrifuged at 5000 rpm for 5 min and residual precursor was discarded.

Single Crystal Growth: To synthesize single crystals, 1.63 g of RbI and 2.3 g of SbI_3 were dissolved in 2 mL of HI. The solution was heated to 373 K for 24 h to dissolve the precursors and then cooled at a rate of 0.014 K min^{-1} to 293 K. The large (5 mm × 5 mm × 5 mm) crystals obtained were cleaned with isopropyl alcohol prior to measurement.

Single Crystal Neutron Diffraction: Time-of-flight single-crystal neutron diffraction was performed on the TOPAZ diffractometer at the Spallation Neutron Source (Oak Ridge National Laboratory).[45] The crystal was mounted on a MiTeGen loop using a small amount of Super Glue. The crystal was measured for approximately 24 h at 295 K using eight sample

orientations with 8e12C of proton charge each. The data collection strategy was obtained with CrystalPlan software.[46] The completeness of coverage of reflections in the reciprocal space was optimized using the orientation matrix obtained from initial sample centering. Peak integration and data reduction were performed in accordance with previously reported procedures.[47] The reduced unmerged data were saved in SHELX HKLF2 format, in which the wavelength is recorded separately for each individual reflection.[48] The neutron structure was solved using JANA2006.[49]

Powder XRD: The nanocrystals were drop cast onto a glass slide for measurement. X-Ray diffraction measurements were conducted using a Rigaku MiniFlex—6G 600 instrument (Bragg-Brentano geometry) equipped with D/teX Ultra silicon strip detector and a Cu K_α radiation source ($\lambda = 1.5406$ Å) operating at a voltage of 40 kV and a current of 15 mA.

Single Crystal XRD: Data were collected on a Bruker Kappa APEX-DUO diffractometer using monochromated Mo-K_α radiation (Bruker Triumph) and were measured using a combination of ϕ scans and ω scans. The data were processed using APEX2 and SAINT (Bruker, 2007). Absorption corrections were carried out using SADABS (Bruker, 2007). The structures were solved with SHELXT (Sheldrick, 2015a) and refined using SHELXL-2016/6 (Sheldrick, 2015b) for full-matrix least-squares refinement that was based on F^2.

XPS: The nanocrystals were drop cast onto a glass slide for measurement. XPS measurements were carried out with the Thermo Scientific K-Alpha XPS system. An Al K_α source with a 400 µm spot size was used for measurements to detect photoelectrons at specific energy ranges to determine the presence of specific elements.

TEM: The one-time washed nanocrystals were centrifuged again at 13 000 rpm for 10 min and the precipitate was collected and redispersed in toluene with the aid of sonication. The specimens were then drop cast on carbon film-coated TEM grids. High-resolution TEM imaging was performed at 300 kV on Hitachi HF 3300 microscope. Data were processed and analyzed by Gatan digital micrograph software.

Optical Characterization: Optical absorption spectra were measured with a Perkin Elmer 950 UV–vis–NIR spectrometer equipped with an integrating sphere for thin-film measurements. PL spectra and PL-decay measurements were carried out using a Horiba FluoroLog-3 spectrofluorometer in reflection geometry under ambient conditions. The sample was excited using monochromated light (375 nm) from a Xenon lamp. The emission was passed through a 500 nm blaze grating monochromator (iHR320) and collected by an infrared photomultiplier tube. For transient-PL measurements, the sample was excited with a 374 nm diode laser at a repetition rate of 10 MHz.

Time-Resolved Photoluminescence (TRPL) Fitting: The PL-decay curves were fit over a 200 ns window for the single crystal, and a 60 ns window for the nanocrystals, with the maximum intensity divided

**ADVANCED
SCIENCE NEWS**

www.advancedsciencenews.com

**ADVANCED
OPTICAL
MATERIALS**

www.advopticalmat.de

by the minimum intensity equaling roughly 1000. The data were fit to a biexponential curve, and when the data were forced to be fit to a triexponential curve, there emerged a third time constant on the order of ≈5–6 ns for both the single crystal and nanocrystal (Figure S6, Supporting Information). However, the overall fit was only marginally improved and a second-order fit was found to be sufficient.

Supporting Information

Supporting Information is available from the Wiley Online Library or from the author.

Conflict of Interest

The authors declare no conflict of interest.

[1] N. J. Jeon, J. H. Noh, Y. C. Kim, W. S. Yang, S. Ryu, S. I. Seok, *Nat. Mater.* **2014**, *13*, 897.

[2] M. I. Saidaminov, J. Kim, A. Jain, R. Quintero-Bermudez, H. Tan, G. Long, F. Tan, A. Johnston, Y. Zhao, O. Voznyy, E. H. Sargent, *Nat. Energy* **2018**, *3*, 648.

[3] L. Zhang, X. Yang, Q. Jiang, P. Wang, Z. Yin, X. Zhang, H. Tan, Y. (Michael) Yang, M. Wei, B. R. Sutherland, E. H. Sargent, J. You, *Nat. Commun.* **2017**, *8*, 15640.

[4] N. Wang, L. Cheng, R. Ge, S. Zhang, Y. Miao, W. Zou, C. Yi, Y. Sun, Y. Cao, R. Yang, Y. Wei, Q. Guo, Y. Ke, M. Yu, Y. Jin, Y. Liu, Q. Ding, D. Di, L. Yang, G. Xing, H. Tian, C. Jin, F. Gao, R. H. Friend, J. Wang, W. Huang, *Nat. Photonics* **2016**, *10*, 699.

[5] D. Shi, V. Adinolfi, R. Comin, M. Yuan, E. Alarousu, A. Buin, Y. Chen, S. Hoogland, A. Rothenberger, K. Katsiev, Y. Losovyj, X. Zhang, P. A. Dowben, O. F. Mohammed, E. H. Sargent, O. M. Bakr, *Science* **2015**, *347*, 519.

[6] X. Gong, O. Voznyy, A. Jain, W. Liu, R. Sabatini, Z. Piontkowski, G. Walters, G. Bappi, S. Nokhrin, O. Bushuyev, M. Yuan, R. Comin, D. McCamant, S. O. Kelley, E. H. Sargent, *Nat. Mater.* **2018**, *17*, 550.

[7] N. J. Jeon, J. H. Noh, W. S. Yang, Y. C. Kim, S. Ryu, J. Seo, S. I. Seok, *Nature* **2015**, *517*, 476.

[8] B. R. Sutherland, A. K. Johnston, A. H. Ip, J. Xu, V. Adinolfi, P. Kanjanaboos, E. H. Sargent, *ACS Photonics* **2015**, *2*, 1117.

[9] Q. Jiang, Y. Zhao, X. Zhang, X. Yang, Y. Chen, Z. Chu, Q. Ye, X. Li, Z. Yin, J. You, *Nat. Photonics* **2019**, *13*, 460.

[10] L. Protesescu, S. Yakunin, M. I. Bodnarchuk, F. Krieg, R. Caputo, C. H. Hendon, R. X. Yang, A. Walsh, M. V. Kovalenko, *Nano Lett.* **2015**, *15*, 3692.

[11] E. Yassitepe, Z. Yang, O. Voznyy, Y. Kim, G. Walters, J. A. Castañeda, P. Kanjanaboos, M. Yuan, X. Gong, F. Fan, J. Pan, S. Hoogland, R. Comin, O. M. Bakr, L. A. Padilha, A. F. Nogueira, E. H. Sargent, *Adv. Funct. Mater.* **2016**, *26*, 8757.

[12] H. Huang, M. I. Bodnarchuk, S. V. Kershaw, M. V. Kovalenko, A. L. Rogach, *ACS Energy Lett.* **2017**, *2*, 2071.

[13] N. Wang, W. Liu, Q. Zhang, *Small Methods* **2018**, *2*, 1700380.

[14] Consolidated Federal Laws of anada, Consumer Products Containing Lead Regulations, https://laws-lois.justice.gc.ca/eng/regulations/SOR-2018-83/page-1.html#h-859286 (accessed: September 2019).

[15] M. Chen, M.-G. Ju, H. F. Garces, A. D. Carl, L. K. Ono, Z. Hawash, Y. Zhang, T. Shen, Y. Qi, R. L. Grimm, D. Pacifici, X. C. Zeng, Y. Zhou, N. P. Padture, *Nat. Commun.* **2019**, *10*, 16.

[16] H. Liu, Z. Wu, J. Shao, D. Yao, H. Gao, Y. Liu, W. Yu, H. Zhang, B. Yang, *ACS Nano* **2017**, *11*, 2239.

[17] X.-G. Zhao, J.-H. Yang, Y. Fu, D. Yang, Q. Xu, L. Yu, S.-H. Wei, L. Zhang, *J. Am. Chem. Soc.* **2017**, *139*, 2630.

[18] A. Swarnkar, V. K. Ravi, A. Nag, *ACS Energy Lett.* **2017**, *2*, 1089.

[19] F. Hao, C. C. Stoumpos, D. H. Cao, R. P. H. Chang, M. G. Kanatzidis, *Nat. Photonics* **2014**, *8*, 489.

[20] L.-J. Chen, C.-R. Lee, Y.-J. Chuang, Z.-H. Wu, C. Chen, *J. Phys. Chem. Lett.* **2016**, *7*, 5028.

[21] T. C. Jellicoe, J. M. Richter, H. F. J. Glass, M. Tabachnyk, R. Brady, S. E. Dutton, A. Rao, R. H. Friend, D. Credgington, N. C. Greenham, M. L. Böhm, *J. Am. Chem. Soc.* **2016**, *138*, 2941.

[22] C. C. Stoumpos, L. Frazer, D. J. Clark, Y. S. Kim, S. H. Rhim, A. J. Freeman, J. B. Ketterson, J. I. Jang, M. G. Kanatzidis, *J. Am. Chem. Soc.* **2015**, *137*, 6804.

[23] M. R. Filip, F. Giustino, *J. Phys. Chem. C* **2016**, *120*, 166.

[24] A. Jain, O. Voznyy, E. H. Sargent, *J. Phys. Chem. C* **2017**, *121*, 7183.

[25] B. Saparov, F. Hong, J.-P. Sun, H.-S. Duan, W. Meng, S. Cameron, I. G. Hill, Y. Yan, D. B. Mitzi, *Chem. Mater.* **2015**, *27*, 5622.

[26] J.-H. Chang, T. Doert, M. Ruck, *Z. Anorg. Allg. Chem.* **2016**, *642*, 736.

[27] K. M. McCall, C. C. Stoumpos, S. S. Kostina, M. G. Kanatzidis, B. W. Wessels, *Chem. Mater.* **2017**, *29*, 4129.

[28] J.-P. Correa-Baena, L. Nienhaus, R. C. Kurchin, S. S. Shin, S. Wieghold, N. T. Putri Hartono, M. Layurova, N. D. Klein, J. R. Poindexter, A. Polizzotti, S. Sun, M. G. Bawendi, T. Buonassisi, *Chem. Mater.* **2018**, *30*, 3734.

[29] F. Jiang, D. Yang, Y. Jiang, T. Liu, X.-G. Zhao, Y. Ming, B. Luo, F. Qin, J. Fan, H. Han, L. Zhang, Y. Zhou, *J. Am. Chem. Soc.* **2017**, *14*, 1019.

[30] Y. Lou, M. Fang, J. Chen, Y. Zhao, *Chem. Commun.* **2018**, *54*, 3779.

[31] J. Zhang, Y. Yang, H. Deng, U. Farooq, X. Yang, J. Khan, J. Tang, H. Song, *ACS Nano* **2017**, *11*, 9294.

[32] B. Yang, J. Chen, F. Hong, X. Mao, K. Zheng, S. Yang, Y. Li, T. Pullerits, W. Deng, K. Han, *Angew. Chem., Int. Ed.* **2017**, *56*, 12471.

[33] A. Wang, X. Yan, M. Zhang, S. Sun, M. Yang, W. Shen, X. Pan, P. Wang, Z. Deng, *Chem. Mater.* **2016**, *28*, 8132.

[34] P. C. Harikesh, H. K. Mulmudi, B. Ghosh, T. W. Goh, Y. T. Teng, K. Thirumal, M. Lockrey, K. Weber, T. M. Koh, S. Li, S. Mhaisalkar, N. Mathews, *Chem. Mater.* **2016**, *28*, 7496.

[35] T. Erdem, H. V. Demir, *Nanophotonics* **2013**, *2*, 57.

[36] H.-W. Chen, R.-D. Zhu, J. He, W. Duan, W. Hu, Y.-Q. Lu, M.-C. Li, S.-L. Lee, Y.-J. Dong, S.-T. Wu, *Light: Sci. Appl.* **2017**, *6*, e17043.

ADVANCED
SCIENCE NEWS
www.advancedsciencenews.com

ADVANCED
OPTICAL
MATERIALS
www.advopticalmat.de

[37] B. Guzelturk, Y. Kelestemur, M. Olutas, S. Delikanli, H. V. Demir, *ACS Nano* **2014**, *8*, 6599.

[38] M. D. Tessier, C. Javaux, I. Maksimovic, V. Loriette, B. Dubertret, *ACS Nano* **2012**, *6*, 6751.

[39] Z. Chen, B. Nadal, B. Mahler, H. Aubin, B. Dubertret, *Adv. Funct. Mater.* **2014**, *24*, 295.

[40] Y. Dang, Y. Liu, Y. Sun, D. Yuan, X. Liu, W. Lu, G. Liu, H. Xia, X. Tao, *CrystEngComm* **2015**, *17*, 665.

[41] L. N. Quan, R. Quintero-Bermudez, O. Voznyy, G. Walters, A. Jain, J. Z. Fan, X. Zheng, Z. Yang, E. H. Sargent, *Adv. Mater.* **2017**, *29*, 1605945.

[42] L. Dou, A. B. Wong, Y. Yu, M. Lai, N. Kornienko, S. W. Eaton, A. Fu, C. G. Bischak, J. Ma, T. Ding, N. S. Ginsberg, L.-W. Wang, A. P. Alivisatos, P. Yang, *Science* **2015**, *349*, 1518.

[43] K. Leng, I. Abdelwahab, I. Verzhbitskiy, M. Telychko, L. Chu, W. Fu, X. Chi, N. Guo, Z. Chen, Z. Chen, C. Zhang, Q.-H. Xu, J. Lu, M. Chhowalla, G. Eda, K. P. Loh, *Nat. Mater.* **2018**, *17*, 908.

[44] Y. Yang, C. Zhang, X. Qu, W. Zhang, M. Marus, B. Xu, K. Wang, X. W. Sun, *IEEE Trans. Nanotechnol.* **2019**, *18*, 220.

[45] L. Coates, H. B. Cao, B. C. Chakoumakos, M. D. Frontzek, C. Hoffmann, A. Y. Kovalevsky, Y. Liu, F. Meilleur, A. M. dos Santos, D. A. A. Myles, X. P. Wang, F. Ye, *Rev. Sci. Instrum.* **2018**, *89*, 092802.

[46] J. Zikovsky, P. F. Peterson, X. P. Wang, M. Frost, C. Hoffmann, *J. Appl. Crystallogr.* **2011**, *44*, 418.

[47] A. J. Schultz, M. R. V. Jørgensen, X. Wang, R. L. Mikkelson, D. J. Mikkelson, V. E. Lynch, P. F. Peterson, M. L. Green, C. M. Hoffmann, *J. Appl. Crystallogr.* **2014**, *47*, 915.

[48] G. M. Sheldrick, *Acta Crystallogr., Sect. C: Struct. Chem.* **2015**, *71*, 3.

[49] V. Petříček, M. Dušek, J. Plášil, *Z. Kristallogr. - Cryst. Mater.* **2016**, *231*, 3.